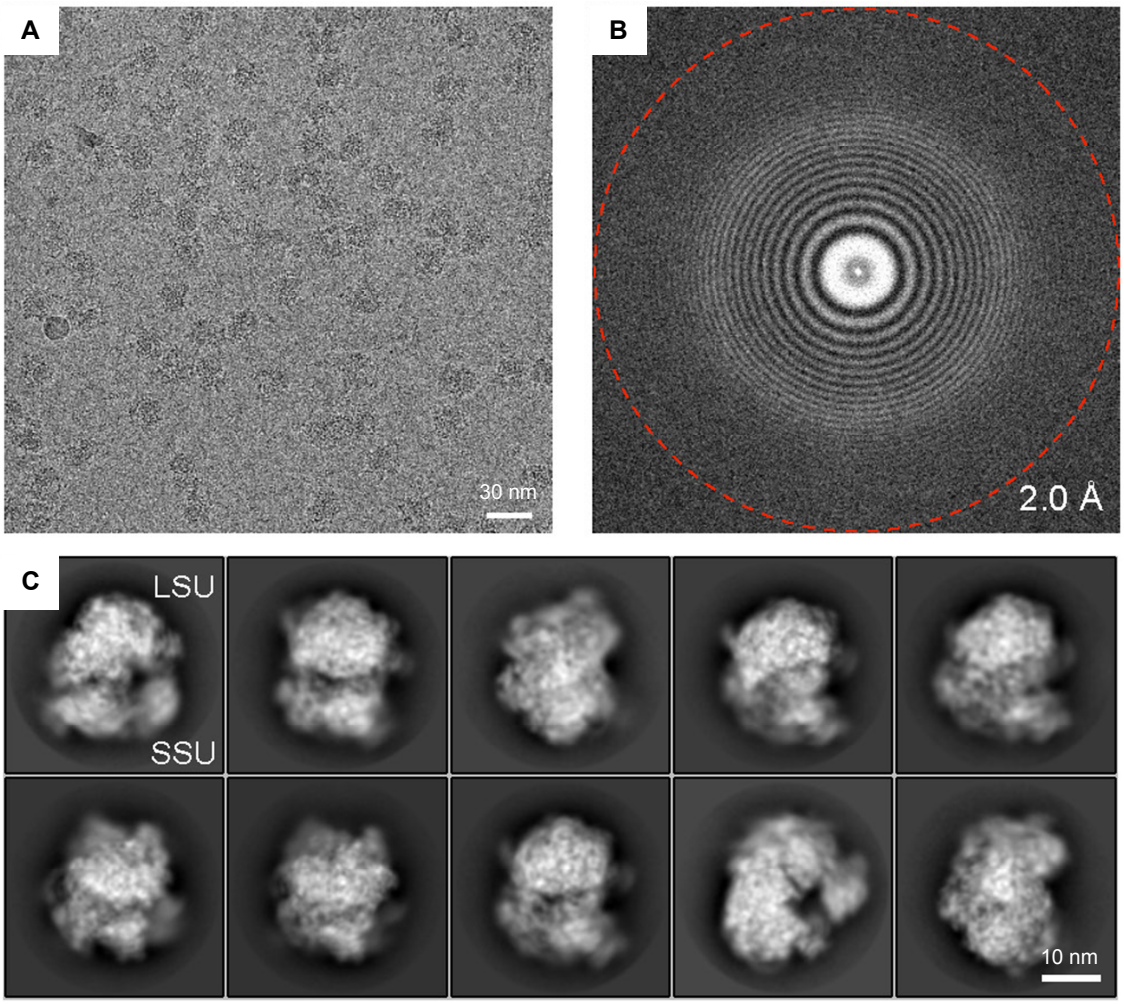

Figure S1: Cryo-EM of *L. donovani* ribosome, related to Figure 1.

(A) Representative cryo-EM micrograph of *L. donovani* ribosome recorded at -0.8 micrometer defocus (scale bar, 30 nm). **(B)** Global power spectrum obtained from the motion corrected micrograph at 1 Å/pixel in **(A)** shows Thon rings up to edge of the spectrum (~2.0 Å, dashed circle in red). **(C)** Representative 2D class averages of the *L. donovani* ribosome showing well defined density for the LSU but blurred out density for the SSU (scale bar, 10 nm).

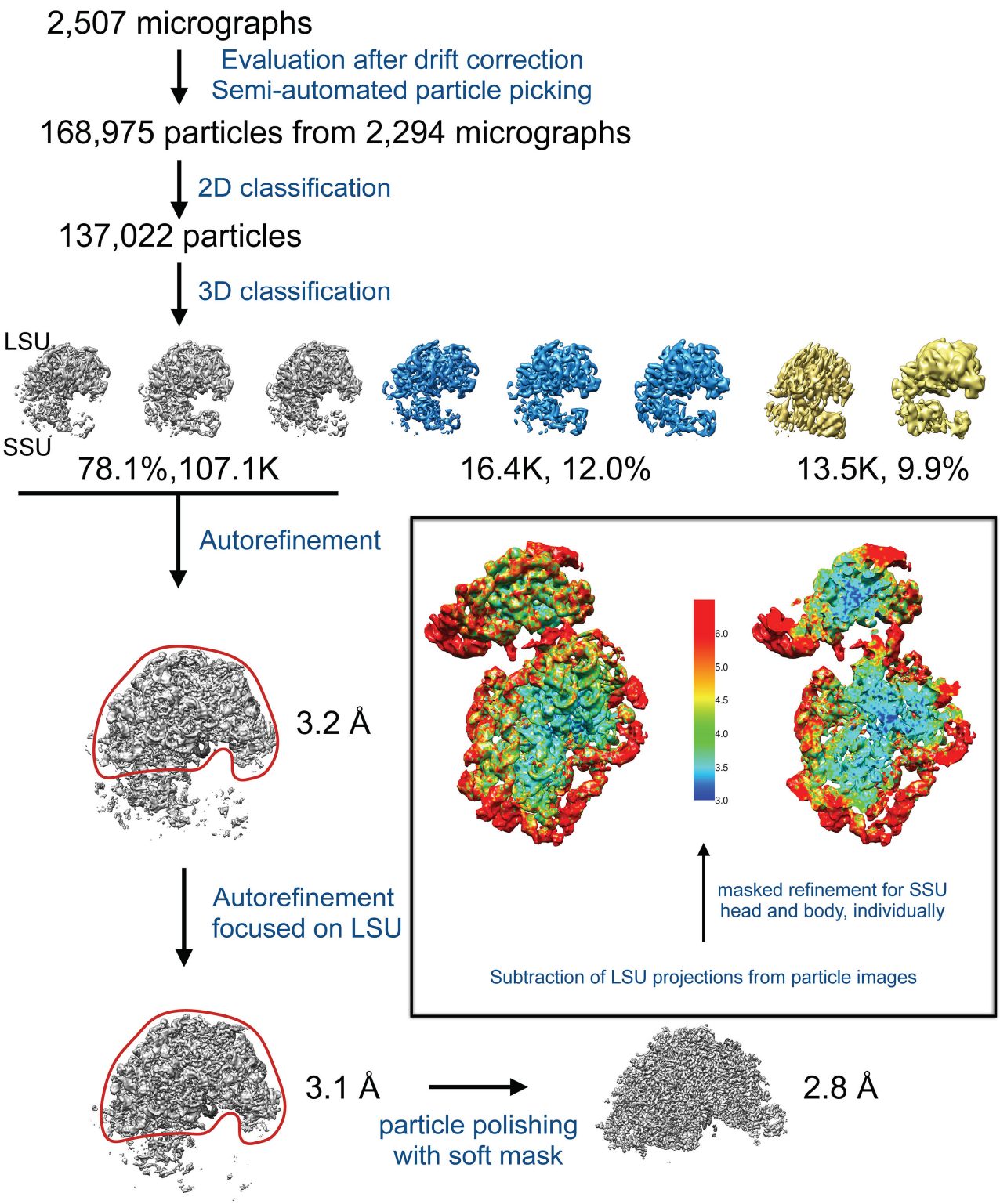

Figure S2: Particle projection selection, classification, and 3D map reconstruction, related to Figure 1.

Flow chart of cryo-EM data processing of *L. donovani* ribosome. Details are provided in the Methods section.

A

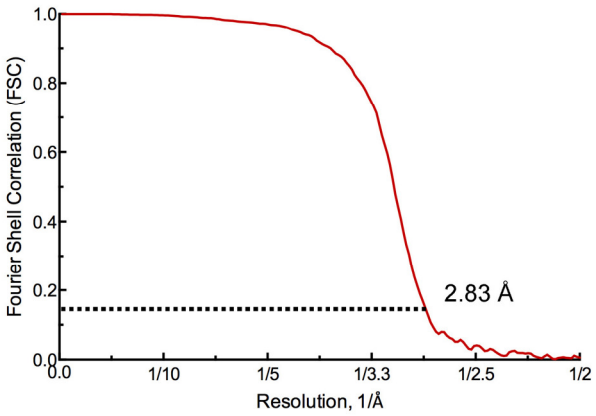

B

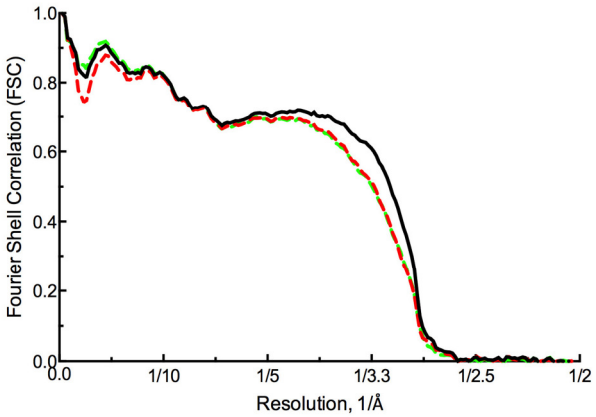

C

Data collection	
Particles	107,134
Pixel size (Å)	0.5
Defocus range (μm)	0.6-2.5
Voltage (kV)	300
Electron dose ($e^-/Å^2$)	30
Refinement	
CC_{map_model}	0.75
Model content	
Total number of atoms	117258
rRNA	73121
rProtein	43884
Solvent (Mg ions/water molecules)	109/144
Model quality	
RMSD	
Bond lengths (Å) / Bond angles (°)	0.007/0.95
Ramachandran plot statistics	
Most favored (%)	88.01
Outliers (%)	0.16
Rotamer outliers (%)	1.41
C-beta deviations	0
RNA Validation	
Correct sugar puckers (%)	96.6
Good backbone Conformations (%)	62.1
Clashscore	24.35
B_iso_{mean}	39.2

Figure S3: Quality of 3D map, comparison to model and data parameters, related to Figure 1.

(A) Gold standard FSC curve for the final 3D map of LSU indicates a resolution of 2.83 Å (FSC=0.143 criterion). **(B)** FSC curves of the final refined model versus the final cryo-EM map (full dataset, black), of the outcome of model refinement with a half map versus the same map (red), and of the outcome of model refinement with a half map versus the other half map (green). The excellent agreement between red and green curves indicates lack of overfitting. **(C)** Cryo-EM data collection and LSU model refinement. Model refinement was performed using *phenix.real_space_refine* (Afonine et al., 2013).

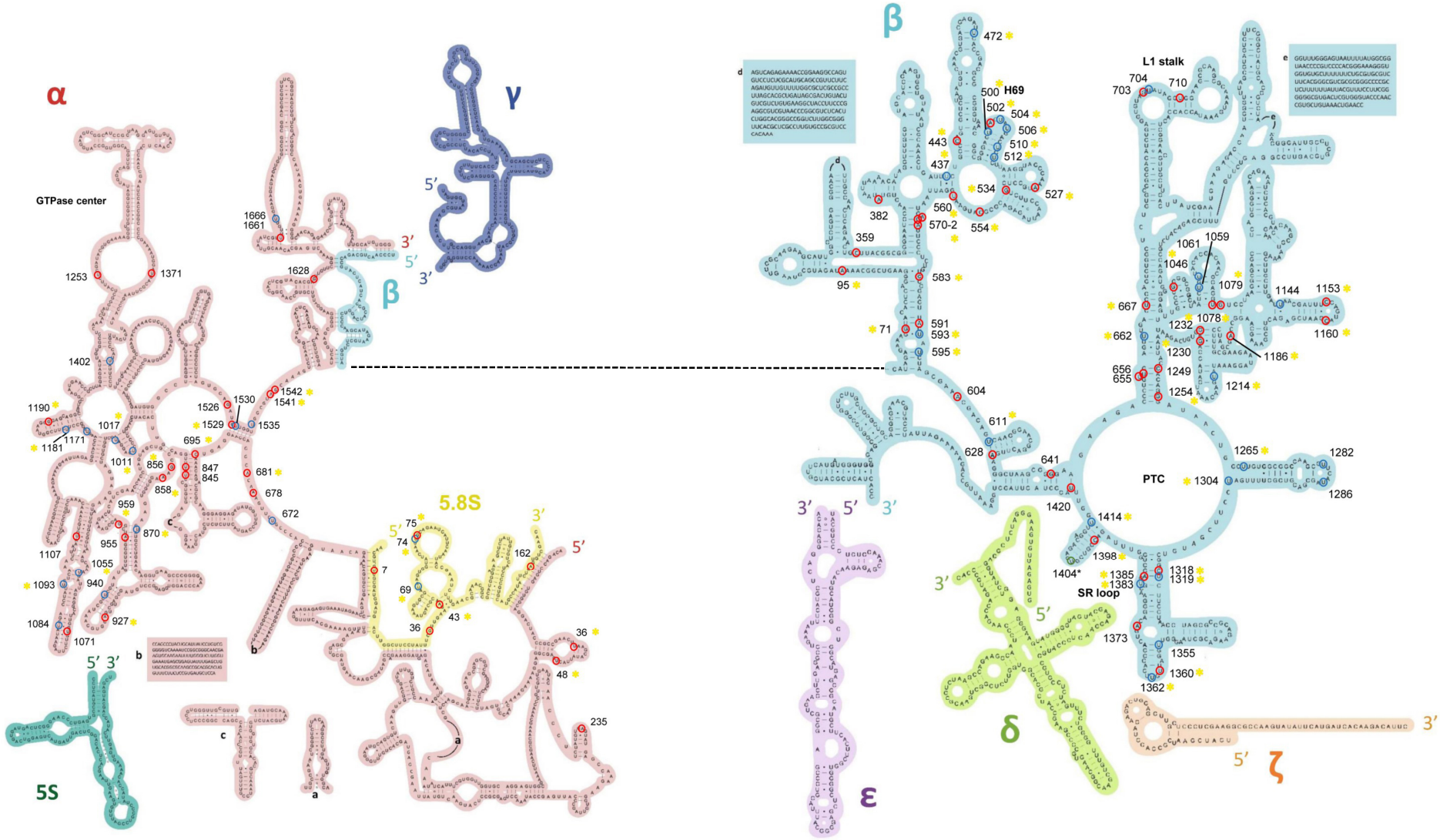

Figure S4: *L. donovani* LSU rRNA 2D maps, related to Figure 2.

Leishmania LSU 2D maps were derived from the 3D cryo-EM map. Ribosomal RNA modifications are highlighted in red (2'-O methylation), blue (pseudouridinylation) and green (dihydrouridine). Conserved positions amongst eukaryotic species are marked in yellow asterisk.

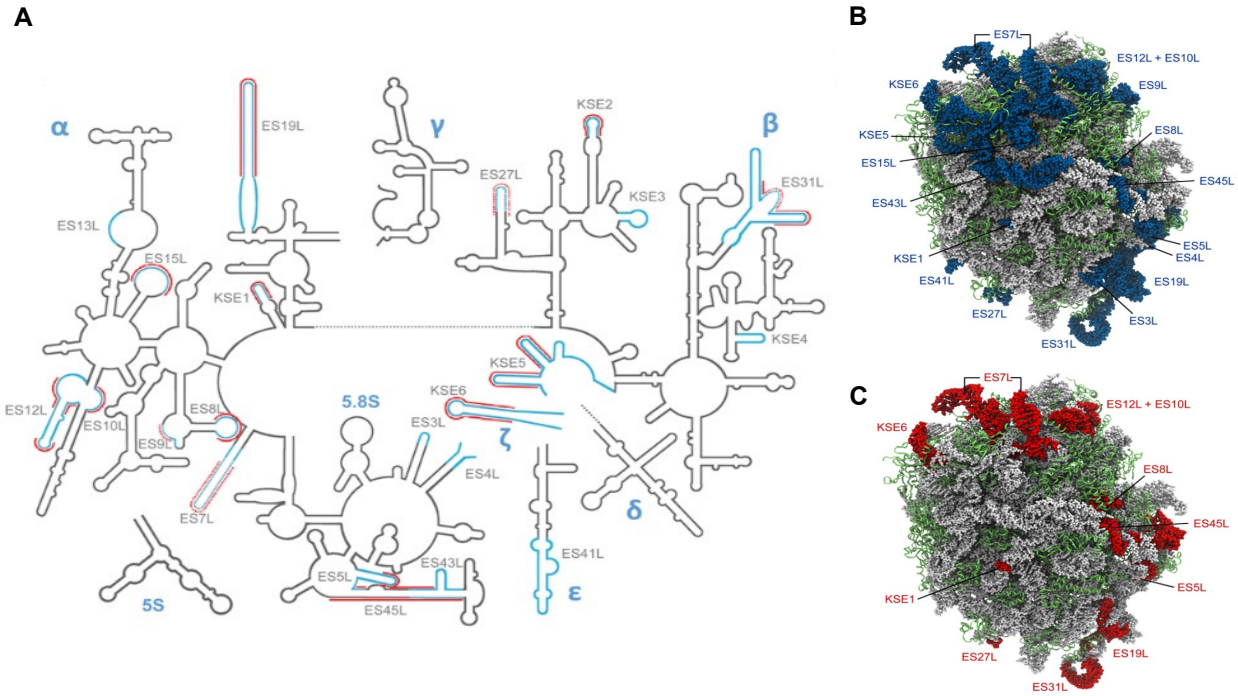

D

Chain	Range	Modeled range	rRNA expansion
α	1-10	3-10	ES4L
	120-150	all range was modeled	ES5L
	196-232	all range was modeled	ES43L
	266-280	all range was modeled	ES45L
	480-654	480-520; 531-571; 633-654	ES7L
	718-730	718-721; 727-730	ES8L
	755-833	all range was modeled	ES9L
	1117-1160	all range was modeled	ES12L
	1250-1260	1253-1260	
	1420-1445	1420-1424; 1432-1445	ES15
	1560-1570	-	KSE1
	1660-1735	1660-1683; 1718-1735	ES19L
β	133-345	133-136; 342-345	ES27L
	465-473	all range was modeled	
	516-533	all range was modeled	
	765-1013	765-872; 938-1013	ES31L
	1197-1210	1197-1199	
	1433-1527	1433-1452	KSE5
ε	45-100	45-47	ES41L
ζ	1-76	1-61	KSE6
5.8S	125-139	125-128; 135-139	ES3L
	160-171	160-169	ES4L

Figure S5: rRNA expansions in *L. donovani*, related to Figure 2.
Secondary **(A)** and tertiary **(B-C)** structures highlighting leishmanial ribosome specific expansions compared to other organisms. Eukaryote specific expansions are highlighted in blue; variable regions amongst kinetoplastids are marked in red **(C)** Tertiary representation highlighting variable regions among different species belonging to the kinetoplastid class. rRNA expansions are colored as in panels **A-B**; ribosomal proteins are shown as light green ribbons. **(D)** *L. donovani* specific rRNA extensions found in the structure with their corresponding numbering range in the chain, their modeled range and their nomenclature. Extension names are according to the *homo-sapiens* nomenclature presented by Anger *et al.* (Anger et al., 2013) (ES - eukaryote specific). Kinetoplastid specific extensions were defined as KSE (kinetoplastid specific extension) and numbered according to their order of appearance in the rDNA gene.

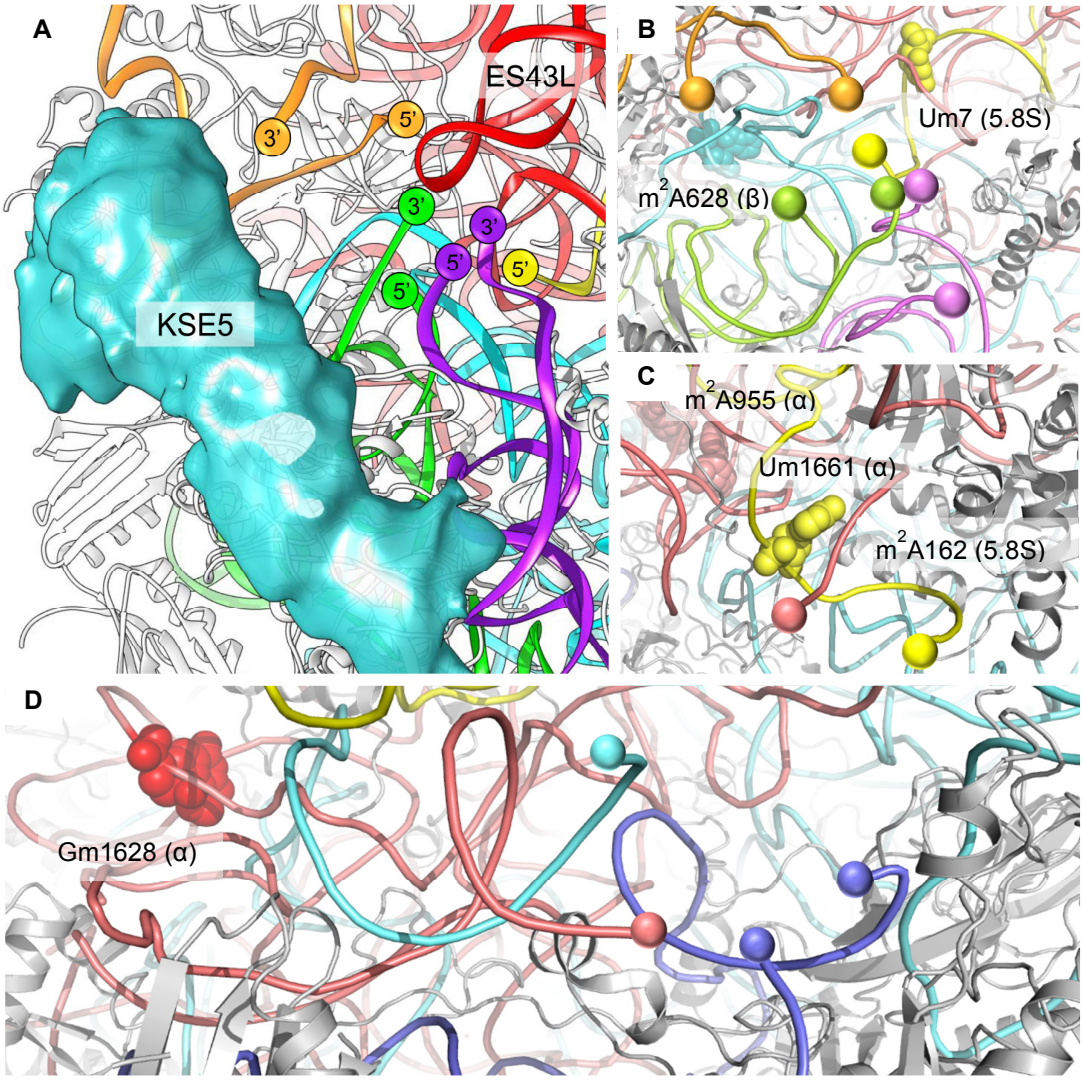

Figure S6: Focal point organization and rRNA modifications in *Leishmania*, related to Figures 3-4.

(A) Seven rRNA chain terminals converge to a focal point (point I) facing the solvent exposed ribosome surface. Two kinetoplastid rRNA extensions, ES43L and KSE5, are located in close proximity to the focal; thus suspected to play an importance in focal point organization or even take part at the kinetoplastid unique cleavage mechanism. ES43L belongs to the alpha chain and is highly extended in kinetoplastids. KSE5 is a kinetoplastid specific rRNA domain located on the 3' end of the beta chain. KSE5 (semitransparent cyan surface) is highly flexible, observed only at low resolution in 3D maps, and was thus not modeled in the structure. Modeled rRNA chains are presented as ribbons with red, cyan, green, purple, orange and yellow for alpha, beta, delta, epsilon, zeta and 5.8S respectively. The high resolution structure enabled the validation of modified RNA residues. Six kinetoplastid specific modifications are spread across focal points I **(B)**, II **(C)** and III **(D)**. Modified residues are highlighted as all-atom-spheres and are colored according to their rRNA chain respective color.

Universal name	Chain ID	Length	Modeled range	Initial model	TritrypDB ID	GR356 seq alternations	MS score (Mascot)
Alpha 26S	1	1782 b	3-1781	4V8P/4V8M/4UGO/De-novo	LdBPK_27rRNA4	-	-
Beta 26S	2	1526 b	2-1451	4V8P/4V8M/4UGO/De-novo	LinJ.27.rRNA1	-	-
Gamma 26S	3	213 b	3-210	4V8P	LdBPK_27rRNA3	-	-
Delta 26S	4	183 b	25-183	4V8P	LinJ.27.rRNA2	-	-
Epsilon 26S	5	133 b	1-133	4V8P	LmjF.27.rRNA.43	-	-
Zeta 26S	6	76 b	1-61	4V8M/De-novo	-	-	-
5.8S	7	171 b	1-169	4V8P	LdBPK_27rRNA5	-	-
5S	8	121 b	1-120	4V8P	LdBPK_23rRNA1	-	-
P0	-	108 aa	-	-	LdBPK_150430.1	-	602.82
P1,P2	-	105 aa	-	-	LdBPK_303780.1	-	1981.39
uL1	-	78 aa	-	-	LdBPK_363950.1	-	1425.56
uL2	A	260 aa	2-246	4V8M	LdBPK_351450.1	-	1100.8
uL3	B	419 aa	5-400	4V8M	LdBPK_323320.1	-	461.9
uL4	C	373 aa	5-305	4V8M	LdBPK_291160.1	-	4788.7
uL5	D	188 aa	9-169	4V8M	LdBPK_220004.1	-	2077.3
uL6	E	190 aa	1-190*	Homology model	LdBPK_211290.1	A189M	2815.1
eL6	F	195 aa	20-195	4UGO	LdBPK_330770.1	-	537.9
eL8	G	348 aa	113-339	4UGO	LdBPK_070550.1	-	4773.5
uL11	-	164 aa	-	-	LdBPK_352230.1	V12I	2766.7
uL13	H	222 aa	21-222	4V8M	LdBPK_340910.1	-	393.67
eL13	I	220 aa	2-133	4V8M	LdBPK_292580.1	A173T; V202A; T219A	163.52
uL14	J	139 aa	12-139	4UGO	LdBPK_353840.1	-	5275.24
eL14	K	233 aa	41-192	4V8M	LdBPK_221370.1	-	974.92
uL15	L	145 aa	2-145	4V8M	LdBPK_353810.1	-	723.71
eL15	M	204 aa	2-204	4V8M	LdBPK_303710.1	-	2914.74
uL16	N	213 aa	1-213*	Homology model	LdBPK_040750.1	R203K	1565.46
uL18	O	305 aa	8-267	4V8M	LdBPK_351870.1	-	1299.83
eL18	P	198 aa	4-198	4V8M	LdBPK_364730.1	-	1538.97
eL19	Q	245 aa	2-157	4V8M	LdBPK_060410.1	-	1214.43
eL20	R	179 aa	4-133	4V8M	LdBPK_350600.1	L158I	1363.47
eL21	S	159 aa	2-150	4V8M	LdBPK_343440.1	-	1711.16
uL22	T	166 aa	2-155	4V8M	LdBPK_240040.1	-	2024.69
eL22	U	122 aa	23-122	4V8M	LdBPK_363430.1	Δ10 aa (N-term)	1319.34
uL23	V	145 aa	27-144	4V8M	LdBPK_060600.1	-	2286.36
uL24	W	143 aa	8-124	4V8M	LdBPK_242140.1	-	602.39
eL24	X	124 aa	2-65	4V8M	LdBPK_361130.1	-	55.22
eL27	Y	134 aa	3-134	4V8M	LdBPK_322850.1	-	1612.83
eL28	Z	147 aa	2-123	4V8M	LdBPK_111110.1	-	758.34
uL29	a	127 aa	3-126	4V8M	LdBPK_262350.1	-	269.04
eL29	b	70 aa	9-70	4VGO	LdBPK_363550.1	-	292.42
uL30	c	252 aa	31-252	4V8M	LdBPK_260160.1	G49A	2059.04
eL30	d	104 aa	11-98	4V8M	LdBPK_350240.1	-	1647.18
eL31	e	183 aa	70-181	4V8M	LdBPK_353340.1	-	1929.41
eL32	f	133 aa	3-128	4V8M	LdBPK_212090.1	T105K	805.97
eL33	g	145 aa	20-144	4V8M	LdBPK_342240.1	-	500.68
eL34	h	168 aa	2-111	4V8M	LdBPK_363930.1	-	296.77
eL36	i	106 aa	38-100	4V8M	LdBPK_210800.1	-	866.33
eL37	j	83 aa	2-79	4V8M	LdBPK_332070.1	-	171.75
eL38	k	83 aa	2-59	4V8M	LdBPK_262230.1	-	604.23
eL39	l	51 aa	2-51	4V8M	LdBPK_161220.1	-	104.41
eL40	m	128 aa	-	-	LdBPK_311930.1	-	96.93
eL41	-	-	-	-		-	-
eL43	n	92 aa	2-92	4V8M	LdBPK_362020.1	-	688.30
eL44	o	106 aa	2-97	4V8M	LdBPK_333380.1		301.46

Table S1: rProtein and rRNA sequence affiliation, modeling and mass spectroscopy, related to main text and Figure 2.
Protein nomenclature has been adopted from *Ban et al.* (Ban et al., 2014). rRNA and rProtein lengths and their modeled range within the cryo EM derived model. Initial models that were used as preliminary guiding templates for model building are listed by their PDB IDs and ribosome model identity. *De-novo* refers to kinetoplastid specific extensions that were manually built in the cryo-EM map without an initial model. Proteins L6 and L16 were built by homology modeling using I-TASSER (Yang et al., 2015) and docked into the cryo-EM map. rRNA and rProtein sequences were derived from a whole genome sequencing of *L. donovani* [MHOM/ET/2009/GR356 clone IV] (unpublished data) and were annotated according to the TriTrypDB**.** Alterations to the published sequences are highlighted. MS Mascot scores for rProteins in the sample used for cryo-EM are also highlighted above.

Modification		Position/Chain [a]	Map sigma level [b]	Prediction in Leish[c]
Am	2'-O-methyladenosine	678/α	3.0	Y
		681/α	3.0	Y
		927/α	2.7	Y
		955/α	2.0	Y
		1541/α	3.0	Y
		382/ β	3.0	Y
		527/ β	3.0	Y
		572/ β	3.0	N
		591/ β	3.0	Y
		604/ β	3.0	Y
		628/ β	3.0	Y
		1186/ β	3.0	N
		162/5.8S	3.0	Y
Gm	2'-O-methylguanosine	856/α	3.0	Y
		959/α	2.0	Y
		1526/α	3.0	Y
		1542/α	3.0	N
		1628/α	3.0	Y
		71/ β	3.0	Y
		534/ β	3.0	Y
		571/ β	3.0	N
		641/ β	3.0	Y
		655/ β	3.0	Y
		1079/ β	3.0	N
		1230/ β	3.0	Y
		1254/ β	3.0	Y
		75/5.8S	3.0	Y
Cm	2'-O-methylcytidine	695/α	3.0	Y
		1529/α	2.5	Y
		443/β	3.0	N
		554/β	3.0	Y
		583/β	3.0	Y
		1160/β	2.0	Y
		1249/β	3.0	Y
		1318/β	2.5	N
		1398/β	3.0	Y
Um	2'-O-methyluridine	36/α	1.6	N
		48/α	1.5	N
		845/α	3.0	Y
		847/α	4.0	Y
		1371/α	2.5	Y
		656/ β	2.0	N
		667/ β	3.0	Y
		1078/ β	2.2	Y
		1153/ β	2.2	N
		7/5.8S	3.0	Y
D	Dihydrouridine	1404/ β	3.0	Y

Table S2: rRNA modifications in *L. donovani* LSU, related to Figure 4.
rRNA modifications in trypanosomatid 67S LSU observed in the density maps. Modified positions **(a)** are presented with relative locations within the rRNA chains. The sigma levels at which each modification is clearly visible are presented in **(b)**. Predictions for *Leishmania* and *Trypanosoma* were adopted from Liang *et al.* (Liang et al., 2005) and Eliaz *et al.* (Eliaz et al., 2015).

Supplemental Experimental Procedures

Parasite handling and ribosome purification

L. donovani [MHOM/ET/2009/GR356 clone IV] promastigotes isolated from the spleen of a VL patient in northern Ethiopia (Zackay et al., 2013) were grown in complete M199 medium containing 10% fetal calf serum at 26˚C to a cell density of $2x10^7$ parasites/mL. Cells were harvested at 4˚C (4000 g), washed 3 times in **resuspension buffer** [45 mM HEPES-KOH pH 7.6, 100 mM KOAc, 10 mM $Mg(OAc)_2$ and 250 mM Sucrose] and then suspended in **buffer A** [45 mM HEPES-KOH pH 7.6, 100 mM K(OAc), 10 mM $Mg(OAc)_2$, 250 mM Sucrose, 5 mM β-mercaptoethanol and a 1:40 dilution of RNasin U (Promega)] to reach a final concentration of $1.5x10^9$ cells/mL. Cell disruption was performed by nitrogen cavitation [90 bar, 45 min, 4˚C] followed by centrifugation steps designed to remove cell debris [30 min at 16,000 g followed by 10 min at 30,000 g, both performed at 4˚C using Ti70 rotor (Beckman)]. Clarified supernatant was gently loaded onto a 1.1 M sucrose cushion in **Buffer B** [20 mM HEPES-KOH pH 7.6, 150 mM KOAc, 10 mM $Mg(OAc)_2$, 1.1 M sucrose and 5 mM β-mercaptoethanol] and centrifuged at 115,800 g at 4˚C for 16.5 h (Ti70 rotor, Beckman). The ribosome enriched pellet was resuspended at 4˚C in **Buffer C** [20 mM HEPES-KOH pH 7.6, 150 mM KOAc, 10 mM $Mg(OAc)_2$ and 5 mM β-mercaptoethanol] and subjected to a 15-30% sucrose gradient centrifugation in **Buffer C** (25,000 rpm, 11 h, at 4˚C on SW28 rotor, Beckman). The 91S peak was collected, and centrifuged at 56,000 rpm for 12 h at 4˚C. The pellet was suspended in **Buffer D** [20 mM HEPES-KOH pH 7.6, 100 mM KOAc, 10 mM $Mg(OAc)_2$, 10 mM NH_4OAc and 1 mM DTT], centrifuged for 1.5 h at 75,000 rpm (Ti100 rotor, Beckman), and the 91S ribosome pellet resuspended in **Buffer D** at a final concentration of 5 mg/mL. Aliquots were flash frozen in liquid nitrogen and stored in -80˚C until further use.

Cryo-EM data acquisition

L. donovani 91S ribosomal samples were diluted to 50 nM and 3.5 µL were applied on glow-discharged holey carbon grids (Quantifoil R2/2, 200 mesh) coated with a continuous thin carbon film. The grids were blotted and plunge-frozen using a Vitrobot Mark IV (FEI Company). Cryo-EM micrographs were collected at liquid nitrogen temperature on a Titan Krios electron microscope (FEI) operating at 300 kV. Micrographs were recorded at a nominal magnification of 29,000X using a K2 Summit direct electron detector (Gatan, Inc.) in super-resolution mode, corresponding to a pixel size of 0.5 Å/pixel, with a dose rate of ~5.0 electrons/$Å^2$/s and defocus values ranging from 0.6 to 2.5 µm. The total exposure time was 6.0 s and intermediate frames were recorded in 0.2 s intervals resulting in an accumulated dose of ~30 electrons per $Å^2$ and a total of 30 frames per micrograph.

Cryo-EM image processing and 3D reconstructions

A total of 2,507 cryo-EM images were recorded during one microscope session. Dose fractionated super-resolution image stacks were binned 2 X 2 and subjected to whole-frame motion correction using MotionCorr (Li et al., 2013). The power-spectra of motion corrected images were evaluated to remove micrographs showing resolution lower than ~3 Å and visible astigmatism, resulting in a working dataset of 2,294 micrographs. A sum of all frames in each image stack was used for further processing. CTF parameters for each micrograph were determined by CTFFIND3 (Sander et al., 2003).

Particle selection, two-dimensional classification and three-dimensional classification were performed on a binned dataset with a pixel size of 2 Å and a box size of 192 X 192 pixels using RELION 1.3 (Scheres, 2012). In total, 168,975 particles were extracted using semi-automated particle selection procedures. In a first step, the particle projections were subjected to reference-free two-dimensional classification in order to identify and discard falsely selected particles or particles categorized in poorly defined classes (**Fig. S1**). The

resulting particle dataset of 137,022 projections was next subjected to unsupervised three-dimensional classification using a 60-Å low-pass filtered cryo-EM map of the yeast *Saccharomyces cerevisiae* ribosome (EMD-1076) as initial reference in order to sort out projections contributing to classes with the most detailed features for the ribosomal large subunit (LSU) (**Fig. S2**). The three-dimensional classification was executed with 8 classes starting with an angular sampling of 7.5°, followed sequentially by angular sampling of 1.8° and 0.9° combined with local angular searches. A total of 107,134 particle projections (78.1% of the input dataset) in the three best defined classes were used for auto-refinement with RELION 1.3 using data with a pixel size of 1 Å, a box size of 384 X 384 pixels, and image stacks including all movie sub-frames. The resulting 3D map (3.2-Å resolution) was subjected to a cycle of focused refinement of the LSU producing a map at 3.1-Å resolution, which was subsequently used for single-particle movie processing (particle polishing) with 3 running averages. In addition, the RELION 1.3 resolution-dependent radiation damage model was used to weigh B-factors for each movie frame. The polished particle projections were used for the final refinement step with a soft mask covering the entire LSU, producing the final map at 2.8-Å resolution.

Given the flexibility of the SSU in respect to the LSU, as observed in 2D classification and map refinement, we employed masked refinement with signal subtraction to improve the resolution for its density. To this end, LSU projections were subtracted from the experimental particle images using the relative orientation of each experimental image from the last refinement of all the polished particles. The resulting experimental images were used for 3D refinement with a soft mask for the body or the head domain, yielding 4.4-Å and 4.8-Å reconstructions, respectively. Local resolution analysis for the SSU showed a range of 3.5-Å resolution in the core to 6 Å in the periphery (**Fig. S2**).

Reported resolutions are based on the gold-standard Fourier shell correlation (FSC) using the 0.143 criterion (Rosenthal and Henderson, 2003) (**Fig. S3**). High-resolution noise substitution was used to correct for the effects of soft masking on the FSC curves. All density maps were corrected for the modulation transfer function (MTF) of the K2 Summit direct detector and then sharpened by applying a negative B-factor that was estimated using post-processing in RELION 1.3. Local resolution was determined using ResMap (Kucukelbir et al., 2014) with half-reconstructions as input maps.

Model building

Model building of the 67S LSU rRNA and proteins was executed by combining template guided and *de-novo* model building. Initial templates of rRNA and protein models were derived from previously reported structures of eukaryotic ribosomes or by homology based predicted models calculated by I-TASSER (Yang et al., 2015). Detailed information on the models used for each ribosomal segment is found in **Table S1**. Initial models were docked as rigid bodies into the cryo-EM maps using Chimera (Pettersen et al., 2004). The docked models were mutated and manually adjusted using COOT (Emsley et al., 2010) real-space and geometry restraint commands to fit into the density maps. The rRNA and protein sequences used for modeling were extracted from the *L. donovani* GR356 whole genome sequence that was annotated based on the *L. infantum* (JPCM5) and *L. donovani* (BPK282A1) genomes deposited at TriTrypDB (Aslett et al. 2010). Accurate sequences for the Ethiopian *L. donovani* strain, showing the differences with the Nepalese reference strain (BPK282A1) are provided in supplemental **Table S1**. Protein content was also examined by MS analysis (**Table S1**). The high-resolution map areas also enabled *de-novo* building of several rRNA domains that differed from the templates. rRNA modifications and solvated ions that were clearly observed in our maps were also modeled. A list of all modified residues is presented in supplemental **Table S2**. Lower resolution areas corresponding to uL6 and uL16, which were clearly observed in our unsharpened maps, were also assigned to the model. Models for uL6 and uL16 were built based on homology using the I-TASSER server (Yang et al., 2015) and were docked to the corresponding EM density. Poorly ordered regions residing on the ribosome periphery were excluded from the final model.

Model refinement and validation

Model refinement was performed using an iterative approach including real space refinement and geometry regularization in COOT (Emsley et al., 2010) combined with real space refinement with PHENIX (Afonine et al., 2013) and its routine *phenix.real_space_refine*. All model components (rRNA, rProteins and solvent molecules) were fit to the map density with simultaneous optimization of stereochemical properties (bond lengths, angles, torsion angles, planarity, etc.) and correction of intra- and inter-molecular clashes.

For atomic coordinate refinement, the final EM map was clipped to a unit cell that accommodated the entire LSU, resulting in an arbitrary unit cell with dimensions of a=b=c=384Å, alpha=beta=gamma=90°, and P1 symmetry. The coarse structure obtained from model building was initially subjected to rigid body refinement as implemented in *phenix.real_space_refine* with each chain (rProtein or rRNA) defined as one rigid body. The entire model was subsequently subjected to real-space refinement using *phenix.real_space_refine* in order to improve the map fitting, the geometry and to avoid clashes. In a next step, map coordinates were Fourier transformed and the resulting structure factor values were used to calculate restrained group temperature factors (two B-factors per residues: one for the main chain and one for the side chain) on the previously refined model. Further model optimization was performed after categorizing the proteins chains according to their CC and their averaged temperature factor values. Proteins L6 and L16, for which homology models were employed, were excluded from these steps and were only included in the final refinement steps for the whole subunit.

In general, protein chains with averaged temperature factor values lower than 20 $Å^2$ were subjected to global and local refinements using *phenix.real_space_refine* (Afonine et al., 2013) and default constrains. Chains with temperature factor values of 20-60 $Å^2$ were refined similarly with tighter r.m.s.d bond length and angle constraints. Protein regions with temperature factor values exceeding 60 $Å^2$ were first submitted to morphing and then to global and local refinements with additional secondary structure constraints.

All rRNA chains were refined together following the same protocol that was used for the low-temperature factor rProteins set. The refined models were subsequently assembled to a unique set of coordinates and submitted to additional refinement cycles in order to improve the interface areas and minimize any inter-molecular clashes. The full LSU model was then subjected to systematic inspection and manual corrections using COOT (Emsley et al., 2010). Finally, the entire structure was validated using Molprobity (Chen et al., 2010) as implemented in Phenix (Afonine et al., 2013) and the correlation coefficients were calculated using *phenix.map_model_cc*. Model overfitting was evaluated through its refinement against one cryo-EM half map. FSC curves were calculated between the resulting model and the half map used for refinement (red curve, **Fig. S3**), as well as between the resulting model and the other half map for cross-validation (green curve, **Fig. S3**). The final refinement statistics are provided in **Figure S3C**.

Liquid chromatography coupled mass spectrometry analysis (LC-MS)

The *L. donovani* 91S sample was loaded into a split-less nano-Ultra Performance Liquid Chromatography apparatus (10 kpsi nanoAcquity; Waters, Milford, MA, USA) and was desalted using a reversed-phase C18 trapping column (180 µm internal diameter, 20 mm length, 5 µm particle size; Waters). Peptides were separated using a T3 HSS nano-column (75 µm internal diameter, 250 mm length, 1.8 µm particle size; Waters) at 0.35 µL/min and eluted into the mass spectrometer. The nanoUPLC was coupled online through a nanoESI emitter (10 µm tip; New Objective; Woburn, MA, USA) to a quadrupole orbitrap mass spectrometer (Q Exactive Plus, Thermo Scientific) using a FlexIon nanospray apparatus (Proxeon). Data was acquired in DDA mode, using the Top20 method. MS1 resolution was set to 70,000 (at 400 m/z) and maximum injection time was set to 20 msec. MS2 resolution was set to 17,500 and maximum injection time of 60 ms. Raw data was processed using Proteome Discoverer v1.4.1.4. MS/MS spectra were searched using Mascot v2.5.1 (Matrix Sciences) and Sequest HT. Data was searched against the *L. donovani* sequences TriTrypDB LdBPK282A1

(http://tritrypdb.org/tritrypdb/). Fixed modification was set to carbamidomethylation of cysteines and variable modification was set to oxidation of methionines and deamidation of asparagines and glutamines. The identifications were filtered such that the global false discovery rate had a maximum of 1%.

Figure preparation

Figures were created using VMD (http://www.ks.uiuc.edu/), PyMol (Schrödinger 2010), and the UCSF Chimera package (Pettersen et al., 2004). Local resolution plots were generated in ResMap (Kucukelbir et al. 2014).

Supplemental References:

Anger, A.M. (2013). Structures of the human and Drosophila 80S ribosome. Nature 497, 80-85.

Aslett, M., Aurrecoechea, C., Berriman, M., Brestelli, J., Brunk, B.P., Carrington, M., Depledge, D.P., Fischer, S., Gajria, B., Gao, X., et al. (2010). TriTrypDB: a functional genomic resource for the Trypanosomatidae. Nucleic Acids Res. *38*, D457-D462.

Ban, N., Beckmann, R., Cate, J.H., Dinman, J.D., Dragon, F., Ellis, S.R., Lafontaine, D.L., Lindahl, L., Liljas, A., Lipton, J.M., et al. (2014). A new system for naming ribosomal proteins. Curr. Opin. Struct. Biol. *24*,165–169.

Chen, V.B, Arendall, W.B., Headd, J.J., Keedy, D.A., Immormino, R.M., Kapral, G.J., Murray, L.W., Richardson, J.S., and Richardson, D.C. (2010). MolProbity: all-atom structure validation for macromolecular crystallography. Acta. Crystallogr. D. Biol. Crystallogr. *66*, 12-21.

Kucukelbir, A., Sigworth, F.J., and Tagare, H.D. (2014). Quantifying the local resolution of cryo-EM density maps. Nat. Methods *11*, 63-65.

Li, X., Mooney, P., Zheng, S., Booth, C.R., Braunfeld, M.B., Gubbens, S., Agard, D.A., and Cheng, Y. (2013). Electron counting and beam-induced motion correction enable near-atomic-resolution single-particle cryo-EM. Nat. Methods. *10*, 584-590.

Pettersen, E.F., Goddard, T.D., Huang, C.C., Couch, G.S., Greenblatt, D.M., Meng, E.C., and Ferrin, T.E. (2004). UCSF Chimera-a visualization system for exploratory research and analysis. J. Comput. Chem. *25*, 1605-1612.

Rosenthal, P.B., and Henderson, R.J. (2003). Optimal determination of particle orientation, absolute hand, and contrast loss in single-particle electron cryomicroscopy. Mol. Biol. *333*, 721-745.

Sander, B., Golas, M.M., and Stark, H. (2003). Automatic CTF correction for single particles based upon multivariate statistical analysis of individual power spectra. J. Struct. Biol. *142*, 392-401.

Schrödinger, L.L.C. (2010). Py-MOL, The PyMOL Molecular Graphics System, V1.8 (2010).

Yang, J., Yan, R., Roy, A., Xu, D., Poisson, J., and Zhang, Y. (2015). The I-TASSER Suite: protein structure and function prediction. Nat. Methods *12*, 7-8.

Zackay, A., Nasereddin, A., Takele, Y., Tadesse, D., Hailu, W., Hurissa, Z., Yifru, S., Weldegebreal, T., Diro, E., Kassahun, A., et al. (2013). Polymorphism in the HASPB repeat region of East African Leishmania donovani strains. PLoS. Negl. Trop. Dis. *7*, e2031.